Catalytic Purification of Directly Written Nanostructured Pt Microelectrodes

Roland Sachser,*[†] Heiko Reith,[†,‡] Daniel Huzel,[†] Marcel Winhold,[†] and Michael Huth[†]

[†]Physikalisches Institut, Goethe-Universität, Max-von-Laue-Strasse 1, 60438 Frankfurt am Main, Germany

[‡]Institute for Microtechnologies (IMtech), RheinMain University of Applied Sciences, Am Brückweg 26, 65428 Rüsselsheim, Germany

S *Supporting Information*

ABSTRACT: In the majority of cases, nanostructures prepared by focused electron beam induced deposition employing an organometallic precursor contain predominantly carbon-based ligand dissociation products. This is unfortunate with regard to using this high-resolution direct-write approach for the preparation of nanostructures for various fields, such as mesoscopic physics, micromagnetism, metaoptical phenomena in the visible spectral range, or others. Following early attempts of postprocessing Pt-based structures prepared by focused electron beam induced deposition at several hundred degrees Celsius in a reactive gas atmosphere, recent

work has focused on developing in situ purification processes by using a stationary O_2 flux in combination with electron irradiation to oxidize the carbonaceous component of the deposits. Here we show that this purification process is driven by the catalytic activity of Pt and in fact does not rely on the parallel electron irradiation process to function, if the O_2 exposure is done in a pulsed fashion. We suggest a multistep cleaning mechanism which results in pure, nanoporous Pt. By suitably chosen beam parameters, high-resolution Pt dot and line structures with dimensions below 10 nm can thus be conveniently obtained. In temperature-dependent resistance measurements, we find the typical metallic behavior of Pt. In low-temperature magnetoresistance measurements, we see clear evidence for weak antilocalization effects and deduce a dephasing length of 234 nm at 1.2 K. We consider this to be a promising starting point for developing this approach into a versatile preparation technique for Pt-based mesoscopic structures, in particular since the purification process can be run in parallel on different deposits. We furthermore anticipate that our results will spur further research on purification approaches for nanostructures prepared by focused electron beam induced deposition containing a catalytically active metal species such as Pd-, Fe-, or Co-based deposits.

KEYWORDS: focused electron beam induced deposition, platinum, nanofabrication, purification, catalysis, in situ conductance measurement
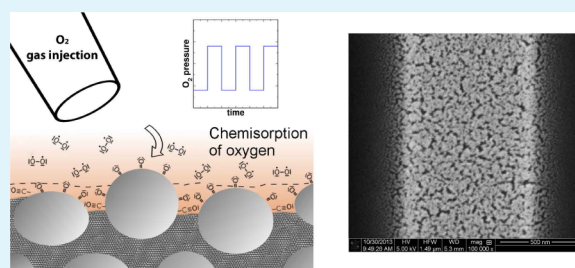
1. INTRODUCTION

Tailored metallic nanostructures form the basis for a wide area of basic and applied research fields. Their fabrication relies mainly on high-resolution electron beam lithography,[1,2] template-based techniques,[3,4] or self-assembly of preformed nanoparticles.[5,6] Although all these techniques are highly sophisticated, for the fabrication of complex shapes focused electron beam induced deposition (FEBID) as a direct-write technique has several advantages, among which are sub 5 nm resolution[7] and the ability to fabricate 3D structures with rather high aspect ratios.[8] However, as a particular type of electron-induced, local chemical vapor deposition, FEBID suffers from the inclusion of organic fragments in the deposits as a consequence of the incomplete dissociation of the commonly used organometallic precursors. The fragmentation pathways are precursor-specific, depend on several different deposition parameters, and have only recently been studied in detail for selected examples.[9,10] Roughly speaking, the prospect of obtaining pure metallic nanostructures directly from FEBID

processes relies on the availability of precursor materials which are specifically suitable for electron-induced full dissociation. So far, very few examples have been identified, all of which are representatives of rather unstable compounds which are difficult to handle in the deposition process.[11,12]

Another approach relies on postprocessing the obtained FEBID structures to remove unwanted carbon-based fragments. Early work in this regard used reactive gas atmospheres, such as oxygen, hydrogen, water vapor, ozone, or hydrogen radicals, at several hundred degrees Celsius to purify, e.g., Pt or Au FEBID structures, usually associated with a pronounced loss of structural integrity due to the volume reduction in the process.[13,14] Recently, in situ postprocessing of Pt(C) FEBID structures obtained from the precursor $Me_3CpMePt$ (Me = methyl; Cp = cyclopentadienyl) by combining stationary

oxygen and water exposure with parallel electron irradiation has been shown to yield virtually pure Pt nanostructures.[15−18] This has been an important step toward establishing FEBID as a direct-write technique for clean metallic nanostructures, albeit predominantly for small-scale fabrication due to the need for parallel focused electron irradiation.

Here we show that the purification process can in fact be performed without electron irradiation; i.e., it can run in parallel on many Pt(C)-based FEBID structures, by employing a pulsed oxygen exposure. By in situ monitoring of the conductance, allowing for a detailed insight into the purification process, we propose a mechanistic explanation based on the catalytic activity of Pt. By careful element composition analysis, we demonstrate the purity of the final Pt structures. In temperature-dependent resistivity measurements, metallic behavior was observed, and from analyzing magnetoconductance data with regard to weak antilocalization effects, a dephasing length of about 234 nm at 1.2 K could be deduced. We anticipate that our results will inspire further research on purification of FEBID nanostructures with catalytically active metal species such as Pd, Fe, or Co, which will likely lead to a substantial extension of the material base for pure metallic nanostructures prepared by focused electron beam induced deposition.

2. EXPERIMENTAL SECTION

2.1. FEBID. FEBID is a versatile bottom-up approach to fabricate nanostructures. A mostly metal−organic precursor is introduced into the vacuum chamber of a scanning electron microscope by a small capillary close to the surface of a substrate on which the precursor adsorbs. When the electron beam is rastered over the surface of the substrate, the adsorbed precursor molecules are dissociated. Volatile components desorb from the surface and are pumped by the vacuum system. The residual components form the later deposit. In this experiment Si/SiO$_2$ (200 nm) substrates with prepatterned Cr/Au electrodes defined by UV lithography were used. The FEBID process was conducted using an FEI Nova Nanolab 600 (equipped with a Schottky-type emitter) at a chamber background pressure of 4×10^{-6} mbar and the metal−organic platinum precursor $(CH_3)_3CH_3C_5H_4Pt$, which was purchased from ABCR with a purity of 99%. The precursor was heated to 44 °C and supplied to the chamber via a capillary with an inner end diameter of 0.5 mm and a tilting angle of 50° to the substrate surface. Thereby the distances to the center of view and to the sample surface were 120 and 100 μm, respectively. For transport measurements, deposits with an area of 32 μm^2 were written in a six-probe geometry. The six-probe deposits (the high-resolution deposits) were written with an acceleration voltage of 5 kV (5 kV, 20 kV for high-resolution samples) at a beam current of 1 nA (0.98 nA, 0.15 nA). A pitch of 20 nm (10 nm, 10 nm), a dwell time of 1 μs (1 ms, 1 ms), and 3000 (20, 20) passes were used. During deposition, the chamber pressure rose to 1.1×10^{-5} mbar.

2.2. Purification Process. A special scanning electron microscope sample holder allowing for temperature control of the sample in the range of 22−350 °C combined with in situ conductance measurements was used. During deposition, the temperature was kept at room temperature. After an additional waiting time to allow the residual precursor molecules to be pumped (2 h), the temperature was increased to 150 °C during a ramp time of 50 min. For the purification process, oxygen was supplied via a homemade gas injection system with an inner end diameter of 0.5 mm at an angle of 15° to the sample surface. The distance was 100 μm to the center of view and 100 μm to the sample surface. Employing oxygen in cycles of about 5 min, the chamber pressure was increased to 1.2×10^{-5} mbar followed by pause cycles of 5 min. The total duration of the purification process was 160 min. On each substrate, four six-probe deposits with a total area of 128 μm^2 were purified at once. Due to the parallel nature of the process, an area of up to about 200 000 μm^2 can be purified in the same time with the setup used.

2.3. In Situ Measurements. For the in situ measurements, a Keithley 2400 SourceMeter and an Agilent 34420A nanovoltmeter were used in conjunction with a multiplexer (Agilent 34970A). Applying a fixed voltage to the structures, four-probe conductance measurements on several samples were performed during the cycling of the purification process.

2.4. Transport Measurements. After preparation, the samples were measured in four-probe geometry in a ⁴He cryostat equipped with a dynamic variable-temperature insert. Temperature-dependent transport measurements were performed at fixed dc current with a Keithley 2636A SourceMeter and an Agilent 34420A nanovoltmeter. For the magnetotransport measurements, higher resolution was needed and ac measurements with a LockIn SRS830 amplifier in conjunction with an SR560 differential preamplifier and a ratio transformer to null the signal at $B = 0$ were used.[19]

2.5. Atomic Force Microscopy. Atomic force microscopy (AFM) was conducted to measure the height of the deposits. A Nanosurf easyScan 2 atomic force microscope with a 70 μm scan head was used. Its D/A converters allow a maximum lateral resolution of 1.1 nm. The maximum resolution in the z direction was 0.21 nm with a typical noise level of 0.8 nm. The used cantilevers PointProbe Plus PPP-NCLR from Nanosensors have a guaranteed tip radius of <10 nm.

3. RESULTS

3.1. Purification and Morphological Characterization. The ability to perform in situ conductance measurements during the purification process, also at elevated temperature, proved to be a key element in identifying the purification mechanism on the basis of previous work.[20] A six-probe geometry for the FEBID structure written between predefined Cr/Au contacts was used, as shown in Figure 1a. As the
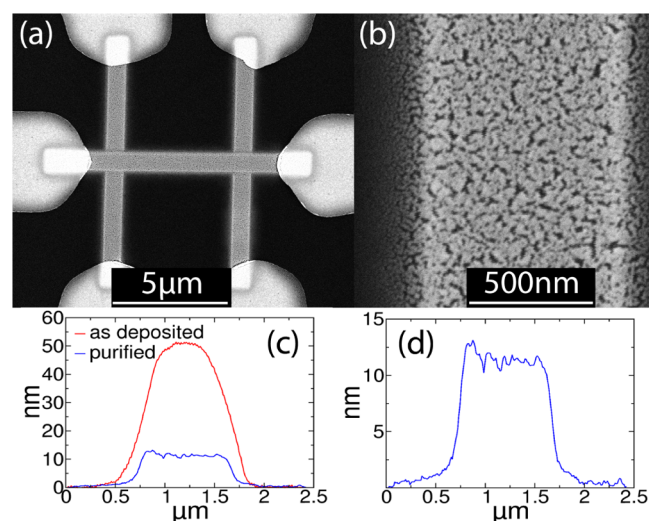

Figure 1. (a) SEM image of a Pt deposit after purification under pulsed oxygen flux at 150 °C written in a six-probe geometry. (b) Magnification of a selected area of (a) showing the nanoporous morphology of purified samples. (c) AFM profiles of the as-grown (red) and purified (blue) structures. (d) Close-up of the AFM profile of the purified structure.

purification process was performed, the conductance of the sample was measured under a fixed voltage bias of 10 mV, resulting in a small electric field of less than 10 V/cm between the outer contact pads. In a series of preliminary experiments done under constant oxygen flux at room temperature and elevated temperature (up to 300 °C) with parallel electron irradiation, we could reproduce the purification effects found in the literature.[15,16] However, in these experiments a pronounced

transient behavior of the conductance under variation of the oxygen flow rate was observed. In particular, we found that under repeated oxygen flux cycling without parallel electron irradiation the strongest relative conductance increases occurred after the oxygen supply was switched off. For selected cycles in early stages of the purification process, we even observed a drop of the conductance under oxygen flow.

In Figure 2 we present the results for a systematic time trace of the conductance during repeated oxygen exposure cylces
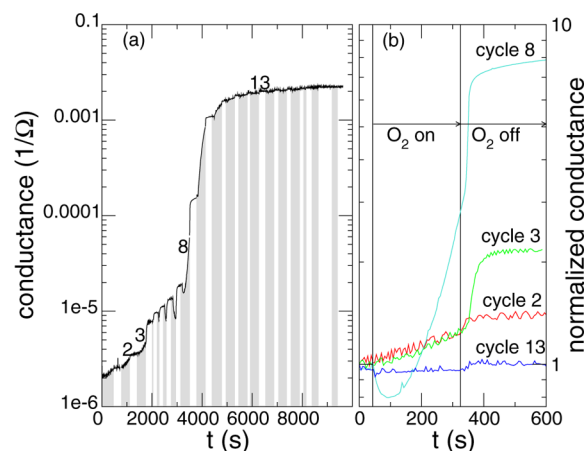
Figure 2. (a) Overview of the measured time-dependent conductance $S(t)$ during the purification process at 150 °C consisting of 19 cycles with a total duration of 160 min. The filled area under the curve shows the intervals with the oxygen flux switched on. (b) Detailed development of conductance for selected cycles 2, 3, 8, and 13, normalized to the conductance at the beginning of each cycle. At about 300 s, the oxygen flux was stopped.

with fixed exposure periods. Several observations are noteworthy. During the first two cycles, the conductance shows a slight increase during oxygen exposure and saturates when the oxygen supply is switched off. For the third cycle, a different behavior is observed. After a slight increase during oxygen flow, the conductance increases by about 50% after the oxygen supply is cut off before, again, saturation occurs. In later cycles, one can even observe a decrease of the conductance during oxygen flow, followed by an increase in the flow-off state. In the final purification stages, the conductance no longer shows any significant changes, independent of the oxygen flow state. In the Discussion, we will come back to these observations in the frame of a mechanistic model of the purification process.

To judge the metal purity after repeated cycling, we analyzed the metal-to-carbon ratio by energy-dispersive X-ray (EDX) analysis. Figure 3 depicts an exemplary EDX spectrum for a purified Pt-FEBID sample on SiO_2/Si. Standard EDX analysis with ZAF correction yields a Pt:C ratio of 71:29. Care has to be taken in interpreting the spectra with regard to this Pt:C ratio due to two systematic error sources. First, for thin structures, a parallel excitation of X-ray fluorescence of the substrate cannot be avoided. This leads to modification of the thin film related X-ray yields and results in systematic errors.[21,22] Second, for structures with high Pt metal content and at excitation energies of 5 keV, low-energy X-ray lines from transitions into the N shell of Pt become visible at about 240 eV. These must not be allocated to the C K line at 277 eV. Here we employed a pure Pt thin film reference sample whose EDX spectrum is also shown in Figure 3. The comparison of the relative intensities of
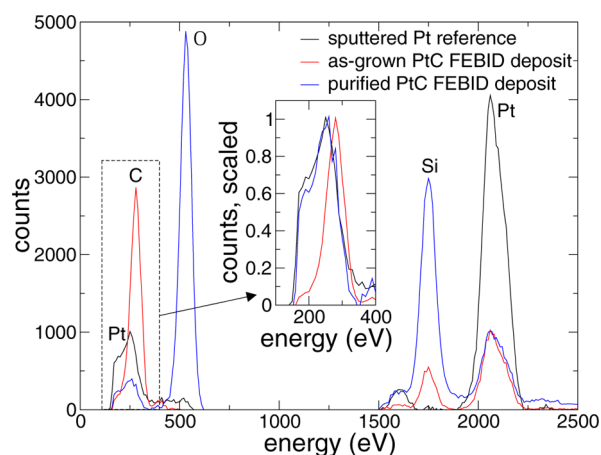

Figure 3. EDX spectra of an as-grown PtC FEBID sample, a PtC FEBID sample purified under oxygen pulses at 150 °C, and a sputtered thin film reference of pure Pt. Inset: magnification of the low-energy peaks scaled to the maximum at 277 eV.

the Pt M, Pt N, and C K lines for an as-grown Pt(C) FEBID structure, a purified Pt(C) FEBID structure, and the Pt thin film reference suggests that the purification results in virtually clean Pt. As is demonstrated by the inset in Figure 3, the spectral peak shapes of the purified Pt FEBID structure and the Pt reference thin film show excellent overlap. This high purity is further reflected in the transport properties of the FEBID structures, which will be presented later.

Now we address the morphology of the purified deposits and also the achievable minimum feature sizes, which are of high relevance for mesoscopic applications. Figure 1b reveals a nanoporous morphology of the purified Pt deposits. Furthermore, a height reduction from 50 ± 1.5 nm for the as-grown PtC deposit to 11 ± 1.5 nm for the purified structure was measured via atomic force microscopy. The void volume fraction of the very thin purified Pt structure can be roughly estimated from a gray scale threshold analysis of the scanning electron microscopy (SEM) image, which yields a value of 0.31 ± 0.07. From these findings, further analysis on the change in morphology, especially the removal of carbon, the volume loss, and the later void volume, can be done (see the Supporting Information).

We note that our results indicate that the void volume fraction $v_{void,f}$ can be reduced by a postgrowth electron irradiation treatment of the as-grown FEBID structure before the purification process is performed. In addition, we point out that the smaller degree of nanoporosity observed for Pt structures which have been purified by a parallel continuous oxygen treatment and electron irradiation is a consequence of the matrix densification effect.[15,20]

We conclude this subsection by showing some preliminary results for high-resolution FEBID Pt structures after pulsed oxygen purification. Figure 4 displays a comparison of the achievable lateral dimensions of purified high-resolution Pt dot and line structures which amount to 12 ± 1.5 and 8 ± 1.5 nm) for acceleration voltages of 5 and 20 kV, respectively. Due to precursor dissociation caused by backscattered electrons, an effect more severe for a low beam energy,[24] unwanted Pt(C) deposition occurs between the line structures, which leads to Pt cluster formation during the purification process. This is clearly noticeable for a 5 keV beam energy and virtually absent for a 20 keV beam energy.
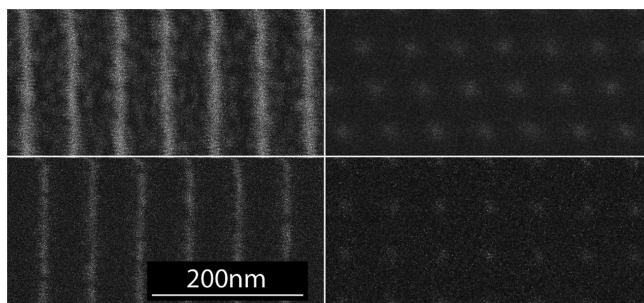
Figure 4. SEM images of line structures (left) and dot lattices (right) written with acceleration voltages of 5 kV (top) and 20 kV (bottom) showing the high resolution achievable in this process. The lines have a distance of 60 nm and a width of 12 nm for the upper image and 8 nm for the lower image.

3.2. Transport Properties.

With regard to the application of Pt nanostructures prepared by the postgrowth purification technique shown here for mesoscopic structures, we studied the low-temperature electronic transport properties of the purified samples. In Figure 5 the temperature-dependent resistivity from
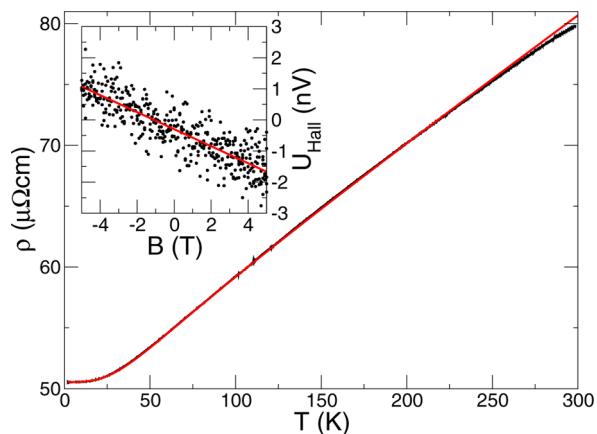
Figure 5. Temperature dependence of resistivity. The red line shows a Bloch−Grüneisen fit with a Debye temperature of 200 K. Inset: linear fit of the Hall voltage with a Hall constant of -1.5×10^{-11} m^3/C.

room temperature to below 2 K is shown. As is to be expected for metallic Pt, the temperature coefficient of resistance is positive. At room temperature we find $\rho(300\ \text{K}) = 79.5\ \mu\Omega$ cm, which is about a factor of 8 larger than that for bulk Pt (10.4 $\mu\Omega$ cm)[25] and in good agreement with previous results obtained for FEBID Pt(C) structures purified under constant oxygen flux parallel to electron irradiation.[15,16] In the present case, we attribute the enhanced room temperature resistivity in part to the smaller effective sample cross-section as a result of the nanoporous morphology. The given values for the resistivity are calculated as an upper limit determined by a homogeneous cross-section with the thickness measured by AFM. Concerning the void volume of 31% estimated from the threshold analysis of the SEM images, a lower limit of 54.9 $\mu\Omega$ cm is given. The RRR (residual resistance ratio) = $\rho(300\ \text{K})/\rho(2\ \text{K}) = 1.57$ is rather small, which is most likely due to strongly enhanced diffusive surface scattering contributions considering the small thickness of 11 nm and, again, the nanoporous morphology. Since finite-size effects in metallic nanostructures can also influence the phonon spectrum and the associated electron−phonon scattering effects,[27] we analyzed

the temperature-dependent resistivity in more detail. For a Bloch−Grüneisen fit, we took in particular sd scattering contributions in Pt into account:[26]

$$\rho(T) = \rho_0 + \rho_{\text{sd}} T^3 \int_0^{\theta_{\text{D}}/T} \frac{x^3}{(e^x - 1)(1 - e^{-x})}\, \mathrm{d}x$$
$$+ \rho_{\text{ss}} T^5 \int_0^{\theta_{\text{D}}/T} \frac{x^5}{(e^x - 1)(1 - e^{-x})}\, \mathrm{d}x \qquad (1)$$

and found the best fit for a Debye temperature of $\theta_{\text{D}} = 200$ K and a residual resistivity of $\rho_0 = 50.54\ \mu\Omega$ cm. For bulk Pt, the Debye temperature calculated from Bloch−Grüneisen fits is reported to be 215 K.[26] We conclude that no significant changes in the electron−phonon scattering channel occur due to the nanoprorous morphology. This is also of relevance with regard to the dephasing mechanisms in the nanostructures, which are presented next.

Magnetoconductance and Hall effect measurements were conducted at various temperatures between 1.2 K and room temperature. In the inset of Figure 5, a representative, virtually temperature-indepedent magnetic field dependence of the Hall voltage from which we deduce a Hall constant of -1.5×10^{-11} m^3/C is shown. Considering the rather high noise level, the results are in quite good correspondence with the Pt bulk value of -2.13×10^{-11} m^3/C.[28] The transverse magnetoconductance at the lowest accessible temperature in our experiment is positive and is clearly indicative of weak antilocalization effects, as is apparent from Figure 6. Quantum interference of time-
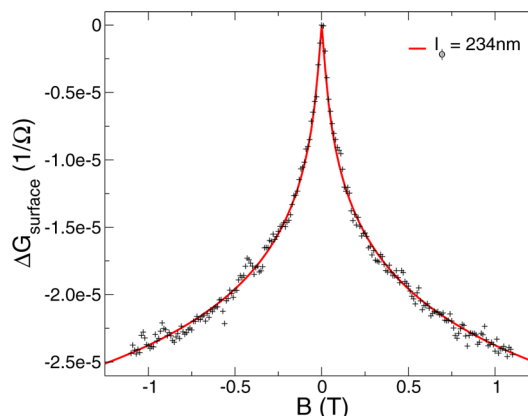
Figure 6. Magnetoconductance at 1.2 K. The red line shows a fit of the weak antilocalization behavior with a coherence length of 234 nm.

reversed states in the presence of strong spin−orbit coupling, as in Pt, leads to an increase of zero field conductance. As a magnetic field is applied, time-reversal symmetry is broken, which causes a small negative magnetoconductance effect. We were able to obtain a satisfying fit of our data (see the solid line in Figure 6) within the Hikami−Larkin−Nagaoka model for two-dimensional systems,[29,30] with the spin relaxation being governed by the Elliott−Yafet mechanism:[31,32]

$$\Delta G(B) = G(B) - G(0) = \alpha \frac{e^2}{2\pi^2 \hbar}[\Psi(1/2 + B_\phi/B)$$
$$- \ln(B_\phi/B)] \qquad (2)$$

The spin−orbit coupling coefficient $-\alpha = 0.5$ and the dephasing field $B_\phi = \hbar/4el_\phi^2$. $\Psi(x)$ denotes the digamma

15871

dx.doi.org/10.1021/am503407y | ACS Appl. Mater. Interfaces 2014, 6, 15868−15874

function. From the fit, we obtain a dephasing length $l_\phi = 234$ nm at 1.2 K.

4. DISCUSSION

In this section we suggest a mechanistic explanation of the Pt(C) purification process under pulsed oxygen conditions based on our time-dependent conductance observations and the known catalytic activity of Pt. As molecular oxygen is dissociatively chemisorbed on metallic Pt, as has been studied in detail,[33] we assume that a thermally activated oxidation of carbon at the Pt/C interface takes place under moderately increased temperatures ($T \approx 150\ °C$) accompanied by the formation of CO. We consider it unlikely that full oxidation to CO_2 can occur with sufficient rates at a process temperature of 150 °C when considering that car catalysts become active at temperatures of about 250−350 °C and typically work at about 600−700 °C.[34] At this point, we note that we did not observe transient behavior in the conductance or a reduction in the Pt:C ratio at process temperatures below about 120 °C. A schematic drawing of the proposed purification process is depicted in Figure 7. To explain the observed conductance vs time trace with this proposed purification process, some additional aspects have to be considered.
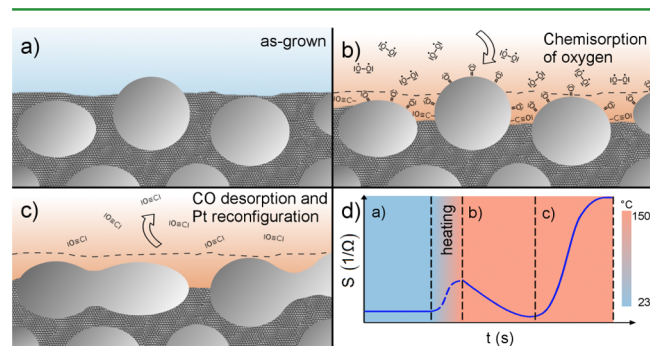
Figure 7. Schematic representation of the PtC purification process. (a) Cross-section of an as-grown nanogranular PtC deposit prepared via FEBID consisting of Pt crystallites with a size of 3−5 nm embedded in a dielectric carbonaceous matrix. (b) PtC deposit under oxygen flux at elevated temperatures ($T = 150\ °C$). The catalytic properties of Pt enable the chemisorption of oxygen, leading to the formation of CO at the Pt/C interface. The desorption of CO, however, is sterically hindered by chemisorbed oxygen. (c) Switching off the oxygen flux is necessary to enable CO molecules to desorb. This process is accompanied by a reorganization of purified Pt grains via surface diffusion, resulting in the formation of a nanoporous structure. (d) Corresponding conductance during the purification process. The chemisorption of oxygen leads to a reduction of conductance due to the removal of the tunneling matrix as well as a decrease of the charge carrier density on the Pt surface. Subsequently, the reorganization of Pt grains triggered by the desorption of CO results in a steep increase of conductance.

During the initial oxygen cycles, the conductance increase is rather slow. We attribute this to the fact that the exposed Pt surface area fraction is small for the as-grown Pt(C) FEBID structures. This is suggested by (cross-sectional) transmission electron microscopy studies which reveal a carbon-rich sheath around the Pt nanograins.[23] As a consequence, the purification process proceeds slowly at the beginning and becomes faster as more and more Pt surface area is exposed. Here an apparent parallel is evident to the activation time needed to initiate area-selective Pt growth by atomic layer deposition on Pt(C) seed

structures.[35] As the purification proceeds, the larger Pt surface area allows for an increasing density of chemisorbed oxygen, which leads to an accelerated oxidation of the carbon at the Pt/C interface. However, under sustained oxygen flux, CO desorption from Pt binding sites is hindered and, in any case, slow at the employed process temperature.[36] The hindering of CO desorption is mainly driven by the small distance between neighboring Pt grains on which the chemisorbed oxygen blocks the pathway for desorbing CO molecules out of the inner part of the deposit. Consequently, the rate of dissociative oxygen chemisorption near the Pt/C interface decreases. This scenario is suggested by the observed saturation behavior in the time-dependent conductance during the oxygen flux-on state. More than that, as long as charge transport between the Pt nanograins is still within the thermally activated tunneling regime, i.e., before direct formation of a percolating path between the nanograins, the conductance change vs time can even be negative (see cycles 2 and 3 in Figure 2b) owing to a reduced tunnel coupling between the grains. Such a reduction may be caused by near-surface charge transfer on the Pt nanograins or changes in the decay length of the electronic Pt surface state wave function. In the next phase of the cycle, as the oxygen flux is turned off, desorption of CO occurs, freeing the Pt surface for oxygen chemisorption in the next cycle. It is also this flux-off state in which the most pronounced reconfiguration of the Pt nanograin assembly toward the final nanoporous morphology is expected to take place. In later cycling stages of the purification process, the conductance is no longer a sensitive monitor for residual carbon, as a dense network of fully developed metallic conductance paths is formed.

We end the discussion by noting that the observed nonmonotonous behavior of the conductance, which we attribute to a varying catalytic activity of Pt, shows clear parallels to the kinetic oscillations in the Pt-catalyzed full oxidation of CO to CO_2 studied in detail by Ertl et al.[37] In these studies, performed under well-controlled ultra-high-vacuum conditions on reconstructed Pt surfaces, the oscillatory catalytic activity was found to be caused by time-dependent variations of the oxygen sticking coefficient.

5. CONCLUSION

In conclusion, we have shown an efficient purification process for Pt(C) nanostructures prepared by focused electron beam induced deposition from the precursor Me₃CpMePt by pulsed oxygen exposure at about 150 °C. In contradistinction to previous purification techniques,[15−17] no parallel electron irradiation is needed, which allows for the treatment of a large number of nanostructures in parallel or, alternatively, of larger surface areas. In this experiment, an efficiency better than 1.25 min/μ^2 was reached to achieve a resistivity $\rho(300\ K) = 79.5\ \mu\Omega$ cm. The obtained purified Pt shows metallic transport behavior and exhibits a dephasing length at 1.2 K of 234 nm. This is highly attractive with a view to applications of this high resolution for the fabrication of mesoscopic structures in studies relying on phase coherence effects. We suggest that the degree of nanoporosity of the Pt structures can be tuned by careful postgrowth electron irradiation treatment before the purification process proper. We therefore anticipate that such nanoporous Pt structures may be highly useful for selective area catalysis applications spanning a lateral scale from a few nanometers to several tens of micrometers. We furthermore can foresee similar processes to be applicable to a wide range of

catalytically active metals, such as Pd (with oxygen) or Fe or Co (with hydrogen), which would substantially enlarge the application range of focused electron beam induced deposition toward pure metallic nanostructures.

■ ASSOCIATED CONTENT

Ⓢ Supporting Information

Further analysis of the change in morphology, especially the removal of carbon, the volume loss, and the later void volume. This material is available free of charge via the Internet at http://pubs.acs.org/.

■ AUTHOR INFORMATION

Corresponding Author

*E-mail: sachser@physik.uni-frankfurt.de.

Notes

The authors declare no competing financial interest.

■ ACKNOWLEDGMENTS

■ REFERENCES

(1) Tobing, L. Y. M.; Tjahjana, L.; Zhang, D. H. Direct Patterning of High Density Sub-15 nm Gold Dot Arrays Using Ultrahigh Contrast Electron Beam Lithography Process on Positive Tone Resist. *Nanotechnology* **2013**, *24*, 075303.

(2) Chandrasekhar, V.; Webb, R. A.; Brady, M. J.; Ketchen, M. B.; Gallagher, W. J.; Kleinsasser, A. Magnetic Response of a Single, Isolated Gold Loop. *Phys. Rev. Lett.* **1991**, *67*, 3578−3581.

(3) Vlad, A.; Mátéfi-Tempfli, M.; Antohe, V. A.; Faniel, S.; Reckinger, N.; Olbrechts, B.; Crahay, A.; Bayot, V.; Piraux, L.; Melinte, S.; Mátéfi-Tempfli, S. Nanowire-Decorated Microscale Metallic Electrodes. *Small* **2008**, *4*, 557−560.

(4) Xu, J.; Chen, L.; Mathewson, A.; Razeeb, K. M. Ultra-Long Metal Nanowire Arrays on Solid Substrate with Strong Bonding. *Nanoscale Res. Lett.* **2011**, *6*, 525.

(5) Grzelczak, M.; Vermant, J.; Furst, E. M.; Liz-Marzán, L. M. Directed Self-Assembly of Nanoparticles. *ACS Nano* **2010**, *4*, 3591−3605.

(6) Jain, T.; Westerlund, F.; Johnson, E.; Moth-Poulsen, K.; Bjørnholm, T. Self-Assembled Nanogaps via Seed-Mediated Growth of End-to-End Linked Gold Nanorods. *ACS Nano* **2009**, *3*, 828−834.

(7) van Kouwen, L.; Botman, A.; Hagen, C. W. Focused Electron-Beam-Induced Deposition of 3 nm Dots in a Scanning Electron Microscope. *Nano Lett.* **2009**, *9*, 2149−2152.

(8) Fernández-Pacheco, A.; Serrano-Ramón, L.; Michalik, J. M.; Ibarra, M. R.; De Teresa, J. M.; O'Brien, L.; Petit, D.; Lee, J.; Cowburn, R. P. Three Dimensional Magnetic Nanowires Grown by Focused Electron-Beam Induced Deposition. *Sci. Rep.* **2013**, *3*, 1492.

(9) Wnuk, J. D.; Gorham, J. M.; Rosenberg, S. G.; van Dorp, W. F.; Madey, T. E.; Hagen, C. W.; Fairbrother, D. H. Electron Induced Surface Reactions of the Organometallic Precursor Trimethyl-(methylcyclopentadienyl)platinum(IV). *J. Phys. Chem. C* **2009**, *113*, 2487−2496.

(10) Wnuk, J. D.; Rosenberg, S. G.; Gorham, J. M.; van Dorp, W. F.; Hagen, C. W.; Fairbrother, D. H. Electron Beam Deposition for Nanofabrication: Insights from Surface Science. *Surf. Sci.* **2011**, *605*, 257−266.

(11) Fernández-Pacheco, A.; De Teresa, J. M.; Córdoba, R.; Ibarra, M. R. Magnetotransport Properties of High-Quality Cobalt Nanowires Grown by Focused-Electron-Beam-Induced Deposition. *J. Phys. D* **2009**, *42*, 055005.

(12) Walz, M. M.; Vollnhals, F.; Schirmer, M.; Steinrück, H. P.; Marbach, H. Generation of Clean Iron Nanocrystals on an Ultra-Thin

SiO$_x$ Film on Si(001). *Phys. Chem. Chem. Phys.* **2011**, *13*, 17333−17338.

(13) Botman, A.; Mulders, J. J. L.; Weemaes, R.; Mentink, S. Purification of Platinum and Gold Structures after Electron-Beam-Induced Deposition. *Nanotechnology* **2006**, *17*, 3779.

(14) Elbadawi, C.; Toth, M.; Lobo, C. J. Pure Platinum Nanostructures Grown by Electron Beam Induced Deposition. *ACS Appl. Mater. Interfaces* **2013**, *5*, 9372−9376.

(15) Mehendale, S.; Mulders, J. J. L.; Trompenaars, P. H. F. A New Sequential EBID Process for the Creation of Pure Pt Structures from MeCpPtMe$_3$. *Nanotechnology* **2013**, *24*, 145303.

(16) Mehendale, S.; Mulders, J. J. L.; Trompenaars, P. H. F. *Nanotechnology 2013: Electronic Devices, Fabrication, MEMS, Fluidics and Computation*, Technical Proceedings of the 2013 NSTI Nanotechnology Conference and Expo, Washington, DC, May 12−16, 2103; ; CRC Press: Boca Raton, FL, 2013; pp 474−476.

(17) Plank, H.; Noh, J. H.; Fowlkes, J. D.; Lester, K.; Lewis, B. B.; Rack, P. D. Electron-Beam-Assisted Oxygen Purification at Low Temperatures for Electron-Beam-Induced Pt Deposits: Towards Pure and High-Fidelity Nanostructures. *ACS Appl. Mater. Interfaces* **2014**, *6*, 1018−1024.

(18) Geier, B.; Gspan, C.; Winkler, R.; Schmied, R.; Fowlkes, J. D.; Fitzek, H.; Rauch, S.; Rattenberger, J.; Rack, P. D.; Plank, H. Rapid and Highly Compact Purification for Focused Electron Beam Induced Deposits: A Low Temperature Approach Using Electron Stimulated H$_2$O Reactions. *J. Phys. Chem. C* **2014**, *118*, 14009−14016.

(19) Beyer, A. D.; Koesters, M.; Libbrecht, K. G.; Black, E. D. Macroscopic Coherence Effects in a Mesoscopic System: Weak Localization of Thin Silver Films. *Am. J. Phys.* **2005**, *73*, 1014−1019.

(20) Porrati, F.; Sachser, R.; Schwalb, C. H.; Frangakis, A.; Huth, M. Tuning the Electrical Conductivity of Pt-Containing Granular Metals by Postgrowth Electron Irradiation. *J. Appl. Phys.* **2011**, *109*, 063715.

(21) Tanji, T.; Yada, K. Fluorescent X-ray Excitation Effect on Quantitative Analysis of Thin Films by EDX. *J. Electron. Microsc.* **1982**, *31*, 300.

(22) Fitzgerald, A. G.; Gillies, A. D.; Watton, H. L. L. A Comparison of the Composition of Thin Films on Substrates Determined by EDX and Surface Analysis. *Surf. Interface Anal.* **1990**, *16*, 163−167.

(23) De Teresa, J. M.; Córdoba, R.; Fernández-Pacheco, A.; Montero, O.; Strichovanec, P.; Ibarra, M. R. Origin of the Difference in the Resistivity of As-Grown Focused-Ion- and Focused-Electron-Beam-Induced Pt Nanodeposits. *J. Nanomater.* **2009**, 936863.

(24) Silvis-Cividjian, N.; Hagen, C. W.; Leunissen, L. H. A.; Kruit, P. The Role of Secondary Electrons in Electron-Beam-Induced Deposition Spatial Resolution. *Microelectron. Eng.* **2002**, *61−62*, 693−699.

(25) Kittel, Ch. *Introduction to Solid State Physics*; Wiley: New York, 1996; p 160.

(26) Poker, D. B.; Klabunde, C. E. Temperature Dependence of Electrical Resistivity of Vanadium, Platinum, and Copper. *Phys. Rev. B* **1982**, *26*, 7012−7014.

(27) Liu, K.; Chien, C. L.; Searson, P. C. Finite-Size Effects in Bismuth Nanowires. *Phys. Rev. B* **1998**, *58*, R14681−R14684.

(28) Greig, D.; Livesey, D. The Hall Coefficient of Dilute Palladium and Platinum Alloys. *J. Phys. F* **1972**, *2*, 699−708.

(29) Hikami, S.; Larkin, A. I.; Nagaoka, Y. Spin-Orbit Interaction and Magnetoresistance in the Two Dimensional Random System. *Prog. Theor. Phys.* **1980**, *63*, 707−710.

(30) Bao, L.; He, L.; Meyer, N.; Kou, X.; Zhang, P.; Chen, Z.; Fedorov, A. V.; Zou, J.; Riedemann, T. M.; Lograsso, T. A.; Wang, K. L.; Tuttle, G.; Xiu, F. Weak Anti-Localization and Quantum Oscillations of Surface States in Topological Insulator Bi$_2$Se$_2$Te. *Sci. Rep.* **2012**, *2*, 726.

(31) Elliott, R. J. Theory of the Effect of Spin-Orbit Coupling on Magnetic Resonance in Some Semiconductors. *Phys. Rev.* **1954**, *96*, 266−279.

(32) Yafet, Y. Conduction Electron Spin Relaxation in the Superconducting State. *Phys. Lett. A* **1983**, *98*, 287−290.

(33) Zambelli, T.; Barth, J. V.; Wintterlin, J.; Ertl, G. Complex Pathways in Dissociative Adsorption of Oxygen on Platinum. *Nature* **1997**, *390*, 495−497.

(34) Kašpar, J.; Fornasiero, P.; Hickey, N. Automotive Catalytic Converters: Current Status and Some Perspectives. *Catal. Today* **2003**, *77*, 419−449.

(35) Mackus, A. J. M.; Thissen, N. F. W.; Mulders, J. J. L.; Trompenaars, P. H. F.; Verheijen, M. A.; Bol, A. A.; Kessels, W. M. M. Direct-Write Atomic Layer Deposition of High-Quality Pt Nanostructures: Selective Growth Conditions and Seed Layer Requirements. *J. Phys. Chem. C* **2013**, *117*, 10788−10798.

(36) Mundschau, M.; Rausenberger, B. Chemical Reaction Fronts on Platinum Surfaces. *Platinum Met. Rev.* **1991**, *35*, 188−195.

(37) Ertl, G.; Norton, P. R.; Rstig, J. Kinetic Oscillations in the Platinum-Catalyzed Oxidation of Co. *Phys. Rev. Lett.* **1982**, *49*, 177−180.